

Order–disorder and ionic conductivity in calcium nitride-hydride

Received: 19 March 2023

Accepted: 5 July 2023

Published online: 20 July 2023

Check for updates

G. J. Irvine¹✉, Ronald I. Smith², M. O. Jones^{1,2} & J. T. S. Irvine^{1,2}✉

Recently nitrogen-hydrogen compounds have successfully been applied as co-catalysts for mild conditions ammonia synthesis. Ca_2NH was shown to act as a H_2 sink during reaction, with H atoms from its lattice being incorporated into the $\text{NH}_3(\text{g})$ product. Thus the ionic transport and diffusion properties of the N–H co-catalyst are fundamentally important to understanding and developing such syntheses. Here we show hydride ion conduction in these materials. Two distinct calcium nitride-hydride Ca_2NH phases, prepared via different synthetic paths are found to show dramatically different properties. One phase (β) shows fast hydride ionic conduction properties (0.08 S/cm at 600 °C), on a par with the best binary ionic hydrides and 10 times higher than CaH_2 , whilst the other (α) is 100 times less conductive. An in situ combined analysis techniques reveals that the effective β -phase conducts ions via a vacancy-mediated phenomenon in which the charge carrier concentration is dependent on the ion concentration in the secondary site and by extension the vacancy concentration in the main site.

Recently, nitrogen–hydrogen (N–H) compounds have attracted interest as potential co-catalysts in mild conditions ammonia synthesis (MCAS: 0.1 MPa, <300 °C)^{1–8}. The long standing issue for MCAS to overcome relates to a scaling relation, due to the saturation of the transition metal (Ru, Co, Ni, and Fe) with adatoms of H_2 , N_2 , and NH_x ^{6,9}. For MCAS, lowering of the activation energy (E_a) of adsorption for reactants (N_2 and H_2) also causes an increase in the adsorption energy (ΔE) of intermediate products (NH_x); the result being that the catalyst's surface is quickly saturated and the overall reaction rate drops dramatically. Recent research has shown that catalytic supports including alkali and alkaline earth metal hydrides (H^-), nitrides (N^{3-}), imides (NH^{2-}), amides (NH_2^-), and nitride-hydrides (N^{3-}H^-) can significantly promote the synthesis of $\text{NH}_3(\text{g})$ ^{3,5,6,8}.

These N–H compounds are proposed to do this by breaking the scaling relationship between H_2 E_a and NH_x ΔE as they have a positive reaction order with respect to $\text{H}_2(\text{g})$. The mechanism that underlies this change is widely believed to result from the transfer of H-adatoms from the TM surface to the N–H compounds⁷; in some cases N-adatoms are additionally transferred^{4,6,10}. This removal of the H and N adatoms frees the catalytic surface for the reaction of NH_x species into in $\text{NH}_3(\text{g})$. Thus, good transport properties, specifically, ionic

conductivity of the support materials are crucially important for the overall heterogeneous system. Recently, several high performing hydride ion conductors (on the order of 10^{-2} S cm^{-1} or better) have been reported in the literature^{11–13}. Both barium hydride and the oxygen doped lanthanum hydride have been reported to show good MCAS activity^{10,14}, while similar oxyhydrides and oxynitride-hydrides to Ba–Li based oxyhydride of Takeiri et al. have also shown good activity^{2,15,16}. This paper reports on a fast H^- ionic conductor: $\beta\text{-Ca}_2\text{NH}$, as well as establishing a nomenclature to distinguish between species of calcium nitride-hydride.

Ca_2NH was first reported by Brice et al. as forming in the $Fd\text{-}3m$ space group with Ca^{2+} ions ($32e$) forming a slightly distorted face-centred cubic close pack arrangement, and the nitride and hydride species occupying the octahedral positions ($16d$ and $16c$, respectively)¹⁷. A 25% intrinsic vacancy concentration due to H ions moving to the $96g$ tetrahedral position was observed. More recently, Verbracken et al. suggested that the structure was better fitted using the $R\text{-}3m$ space group, which differs from the $Fd\text{-}3m$ in the ordering of the octahedral positions¹⁸. Additionally, they found a 13% intrinsic vacancy concentration at ambient temperature. The $R\text{-}3m$ space group is also observed for the barium and strontium analogues^{19,20}. Finally,

¹Chemistry, University of St Andrews, St Andrews, Scotland KY16 9ST, UK. ²ISIS Neutron and Muon Source, Rutherford Appleton Laboratory, Oxford, England OX11 0QX, UK. ✉e-mail: gji4@st-andrews.ac.uk; jtsi@st-andrews.ac.uk

Verbracken et al. noted the presence of a secondary *quasi-imide phase* that constituted approximately 10% of their system. This phase disappeared upon heating. Sichla et al. and Chemnitzer et al. observed previously that the nitride-hydrides of Sr form mixed phases containing nitride, hydride, and imide anions^{20,21}. Additionally, these types of systems have been observed and studied in lithium NH compounds^{22,23}. These disordered phases comes in many forms depending on the synthesis route. A paper by Weidner et al. gives a considered discussion around these *quasi-imide phases*²⁴. Importantly, the disruption in site occupancy in these mixed phases posed a significant challenge for the application of these materials in reversible solid-state hydrogen storage²⁴. Makepeace et al. suggest that a compositional compromise must be struck in cycling lithium imide to lithium amide during ammonia synthesis as the prior has significantly better electrical performance than the latter²³.

We are aware of four approaches to produce calcium nitride-hydride and have summarized these in Supplementary Table 2. Importantly, depending on method, the system can either contain or not contain a secondary anion species (we label these phases α - and β - respectively). Here, we show the effect the presence of the secondary species and associated loss of ordering has on structure and electrical properties of the system.

Two precursors that had been previously shown to react with N_2 and H_2 gases were chosen: a hydride^{3,6,10,25} (CaH_2) and a nitride (α - Ca_3N_2)^{26,27}. These compounds were heated to 600 °C under flowing 5% H_2/D_2 and N_2 in Ar respectively. The properties of the resulting phases were analysed from data collected from in situ neutron powder diffraction (NPD) collected on Polaris Diffractometer at ISIS²⁸ and impedance spectroscopy (using a specialized neutron rig (see Irvine et al.²⁹). Details of these analyses are available in the Supplementary Methods. Next, the $CaH_2(D_2)$ system was exposed to N_2 gas, while the α - Ca_3N_2 system was exposed to H_2/D_2 . The result in both systems was the emergence of a Ca_2NH phase.

Figure 1a shows the final NPD patterns from the two experiments with quite different phases being produced. Starting from α - Ca_3N_2 (94 wt% with a 6% CaO impurity, see Supplementary Figure and Table 1) a fairly simple Ca_2NH pattern is produced without any evidence of secondary phases. The resulting phase exhibits a pattern that is shifted towards larger d-spacings and has lost the peaks associated with the octahedral ordering in the $Fd-3m$ and $R-3m$ space groups (see Supplementary Figs. 2–4 and accompanying discussion). This loss of ordering allows for the indexing of Ca_2NH in the rock-salt structure space group ($Fm-3m$). This space group assignment has a lattice parameter that is half the size for the analogous structure using the Fd -

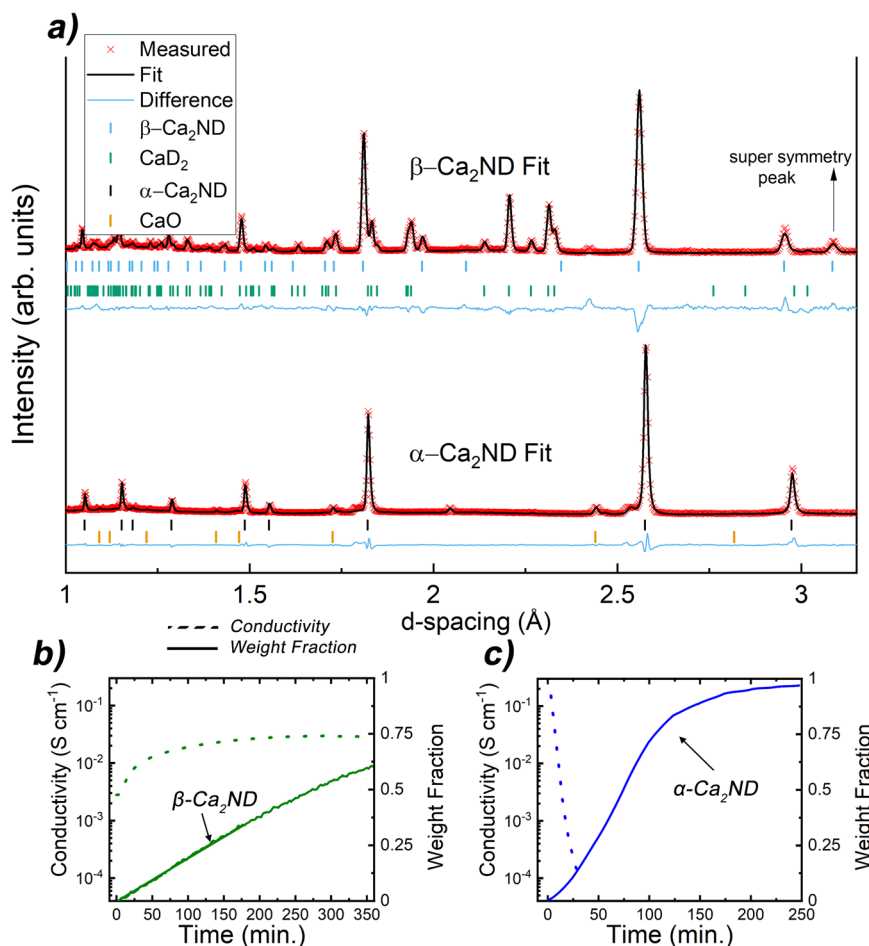


Fig. 1 | Neutron powder diffraction (NPD) fit and conductivity results. a NPD patterns of the α - and β - phases (from α - Ca_3N_2 and CaH_2 precursors respectively) of calcium nitride hydride(deuteride) collected on Polaris diffractometer at ISIS. The patterns show that the α -phase loses the extra peaks associates with $Fd-3m$ space group. This symmetry relates to the ordering of the anionic octahedral positions. **b, c** Total conductivity of the system and weight fraction of the Ca_2ND phases

versus time. Solid line is weight fraction and dotted line conductivity. EIS data collected for α -phase system was done in a separate experiment that matched the conditions of the Polaris experiment. The β -phase system EIS data was collected simultaneously with the NPD data. Results show that as the α -phase emerges the measured conductivity plummets by 3 orders of magnitude while the emergence of the β -phase is associated with an increase in conductivity.

3*m* assignment. The best fit was produced by placing the Ca²⁺ ions in 4*a* position and N³⁻ and D⁻ (deuteride) ions in the 4*b* position. Furthermore, a 20% concentration of imide (NH²⁻) protons were placed in the 24*e* position which correspond to proton positions in the published calcium imide structure³⁰. Thus, the reaction of α-Ca₃N₂ with H_{2(g)} at 600 °C produces a mixed/disordered phase which we label α-Ca₂NH. We also note that similar to other systems containing secondary anion species^{18,23}, the system exhibits pronounced asymmetric peaks upon cooling (see Supplementary Fig. 5). Additional experiments showed that α-Ca₃N₂ only begins to react to α-Ca₂NH at temperatures >450 °C (see Supplementary Fig. 6 and Supplementary Table 4), and if heated to 800 °C can be fully converted to CaNH (see Supplementary Fig. 7 and Supplementary Table 5).

There are a large number of extra peaks present in the sample produced from CaD₂ (pure at the start of the experiment) as a result of a phase equilibrium between the produced Ca₂ND phase and the N-doped CaD₂ precursor (see Supplementary Figs. 8, 9, and Supplementary Table 6). Whilst the residual content is decreasing with time, its content is not tending to zero, hence an equilibrium mixture is being approached.

The Ca₂ND phase does not show the disordering observed in an α-phase and was indexed and fitted using the *Fd-3m* space group and model proposed by Brice et al.¹⁷, nor does it show any evidence of a secondary anion species and thus the phase is labelled β-. The relative lattice parameters for two phases are 10.3001(12) Å vs 10.23062(24) Å for the α- and β-phases, respectively. Previous research has shown that solid solutions of NH compounds have larger lattice parameters than the pure compounds in agreement with the findings here^{24,31,32}.

The β-phase agrees well with the result published by Brice et al.¹⁷. Full refinement yielded an occupancy of the D1 octahedral site of 0.822(11) as opposed to the value of 0.75 reported by Brice et al., with the remainder being located in a tetrahedral site (18.9%, as opposed to 25% previously published) giving a stoichiometric compound (Ca₂NH_{0.997(34)}). One major difference between the fit in this paper and that of Brice et al. is the position of the D2 site. It was found that refinement of the 9*6g* position proposed by Brice et al. was unstable and required that the atomic displacement parameter (ADP), occupancy, and coordinates be fixed. Using the 48*f* position instead allowed for the full refinement of the position, although the low occupancy and high multiplicity create larger than normal errors. A comparison between the fit results of the two phases is shown in Table 1. Further experiments revealed that the synthesis of Ca₂NH from CaH₂ required temperatures above 400 °C. Additionally, heating β-Ca₂NH to 800 °C resulted in the appearance of shoulder peaks (in a post experiment powder x-ray diffraction pattern, see Supplementary Fig. 7) associated with secondary anionic species.

Next, we explore the effect the order versus disorder has on the electrical properties of the systems.

Electrochemical Impedance spectroscopy (EIS) data collected during the reaction of CaD₂ with N₂ showed that as the experiment proceeded, measured conductivity increased by an order of magnitude from 3 × 10⁻³ S cm⁻¹ to 3 × 10⁻² S cm⁻¹ (see Fig. 1b). The rise in conductivity observed correlated with the increasing content of the β-Ca₂ND phase. A separate experiment found that doping of CaH₂ with N₂ resulted in an increase in measured conductivity from 5.63 × 10⁻³ S cm⁻¹ to 5.8 × 10⁻² S cm⁻¹ while the post-experiment x-ray diffraction pattern showed a 9:1 ratio of β-Ca₂NH to CaH₂ (see Supplementary Fig. 10). Previous work also showed that the precursor CaH₂ had an ionic conductivity on the order of 10⁻³ S cm⁻¹ at 600 °C³³. The difference in conductivities would influence ammonia production where hydrogen flux from the hydride becomes limiting, noting that in the systems shown by Hattori et al.: CaH₂ and Ca₂NH mixed with Ru at 340 °C produced ammonia at similar rates where the better conducting Ca₂NH system had significantly less Ru catalyst by weight³.

For the α-phase, a second experiment conducted at the University of St Andrews that replicated the experimental conditions of the

Polaris experiment (with H₂ instead of D₂) found that the upon reaction of α-Ca₃N₂ with hydrogen, the measured conductivity plummeted by 4 orders of magnitude (from 10⁻¹ S cm⁻¹ to 10⁻⁴ S cm⁻¹, see Fig. 1c). Note that α-Ca₃N₂ showed good conductivity properties in accord with electronic semiconductor behaviour (see Supplementary Fig. 11). Thus, the EIS data shows that the α-phase has poor electrical properties, while the β- is a potential fast ion conductor, similar to previously published results for Ba₂NH^{19,34}.

To further explore the structural difference between the two phases, NMR and Raman spectra were collected at room temperature. Figure 2a, b shows the NMR and Raman, respectively. The NMR ¹H peak at 5.2 ppm is relatively broad for the α-phase compared to the β-. Broadening of this type can result from dynamic motion or static disorder³⁵. In this case, it is likely the result of static disorder as the spectra were collected at room temperature. The relative disorder of the α- mirrors the results from the NPD study that showed that the α-phase octahedral sites lacked the ordering found in the β-phase causing a change in symmetry and formation in the rock salt structure. Furthermore, the α-phase NMR shows the existence of secondary hydrogen species associated with amide (NH₂) at 1.0 ppm and imide at (NH²⁻) at -2.7 ppm. The amide appears more prevalent in the spectrum due to the fact that its peak is quite sharp compared to the imide which is not only positionally distributed around the bonded N atom, but also randomly distributed throughout the host lattice. The final peak at -1.3 ppm is thought to be associated with OH⁻ groups formed during loading and unloading the sample into the NMR instrument.

Raman data also show broadening in the α-phase spectrum for the peaks associated the nitride-hydride species (292 cm⁻¹)⁷. This peak is also shifted to lower wavenumbers as compared to the β- (328 cm⁻¹) suggesting that the configuration of the α-phase is lower energy. This result matches well with published results on disordered lattices^{22, 36}. The α-phase also shows the characteristic broad peaks between 100 and 1000 cm⁻¹ of the imide species, as well as the sharp peak at 3125 cm⁻¹^{7,22}.

Together, the NMR and Raman data confirm the NPD data structure refinement results that the α- exhibits disorder and contains a concentration of imide species while the β- is relatively ordered at room temperature with a single NMR signal implying thermally induced defects.

The β-phase conductivity was explored further on Osiris spectrometer at ISIS³⁷. A pellet of CaH₂ was loaded into the specialized in situ rig. The sample was exposed to short 5 min doses of N₂ in Ar and H₂ (5/90/5 cm³ min⁻¹ respectively) at 600 °C. NPD patterns were collected before and after each dose, while EIS and quasi-elastic neutron scattering (QENS) data were collected over the course of several hours. Further details and example data and fits are available in Supplementary Figs. 12–14. Data sets are labelled *N* followed by a numeral representing the dose number, while the number after the hyphen is the dataset for that dose.

The first measurable broadening of the quasi-elastic data came after the 4th nitrogen dose and the second QENS dataset (labelled N4-2 in Fig. 3). This dose also saw the first significant rise in the phase fraction of β-Ca₂NH as measured by NPD as well as a jump in the measured ionic conductivity as measured by EIS (σ_{EIS}) (Fig. 3). Thus, the β-Ca₂NH phase is again correlated with the rise in σ_{EIS} . Additionally, the associated QENS broadening strongly suggest that the increase in σ_{EIS} is associated with ionic diffusion of hydrogen, in this case likely H⁺ ions. The QENS data were modelled by the Chudley-Elliott jump diffusion model (CEM)³⁸ which produces two important physical characteristics of the diffusion process: the jump length (*l*), and the residence time (τ). In order to understand the mechanism of diffusion it is important to contrast the extracted *l* with site to site distances. Figure 4 shows a plot of different site to site distances from the β-Ca₂NH phase refinement of the Osiris diffraction patterns as well as the

Table 1 | Comparison between α - and β -phase fits from neutron powder diffraction data

NPD Data @ 600 °C		α -Ca ₂ NH (Fm-3m) [Ca ₂ N _{0.8} D _{0.8} (ND) _{0.4}]					
a (Å)	5.15005 (6)	Ca (0,0,0)		D1 (½,½,½)		D2 (x,y,z) -imide proton	
Volume (Å ³)	136.5945 (28)	Fraction	1 ^f	Fraction	0.4 ^f	x	0
		Uiso x100 (Å ²)	3.317 (30)	Uiso x100 (Å ²)	2.258 (20)	y	0
wRp	0.0288			N1 (½,½,½)		z	0.35 ^f
Rp	0.0412			Fraction	0.6 ^f	Fraction	0.0333 ^f
χ^2	7.262			Uiso x100 (Å ²)	2.921 (20)	Uiso x100 (Å ²)	3.00 ^f
		β -Ca ₂ NH (Fd-3m) [Ca ₂ ND _{0.997}]					
a (Å)	10.23062 (24)	Ca (x,x,x)		D1 (0,0,0)		D2 (x,y,z) -hydride	
Volume (Å ³)	1070.79 (4)	x	0.26171 (11)	Fraction	0.808 (10)	x	0.125 ^f
		Fraction	1 ^f	Uiso x100 (Å ²)	5.73 (16)	y	0.125 ^f
wRp	0.0177	Uiso x100 (Å ²)	1.73 (4)	N1 (½,½,½)		z	-0.0904 (30)
Rp	0.0308			Fraction	1 ^f	Fraction	0.063 (11)
χ^2	4.889			Uiso x100 (Å ²)	2.030 (29)	Uiso x100 (Å ²)	5.39 (53)

The α -phase is associated with loss of symmetry in the anionic sublattice. Furthermore, the two phases have distinctly different secondary D sites; the α - being characteristic of an imide proton, while the β - is a tetrahedral coordinated hydride site. The imide concentration of the α - phase is 20%, while the tetrahedral site of the β -phase has a 18.9% concentration. The actual stoichiometry of the phases are given in brackets. Parameters fixed for the refinement are denoted with a superscript f. Standard errors are reported in parentheses. Additional fitting statistics available in Supplementary Table 3.

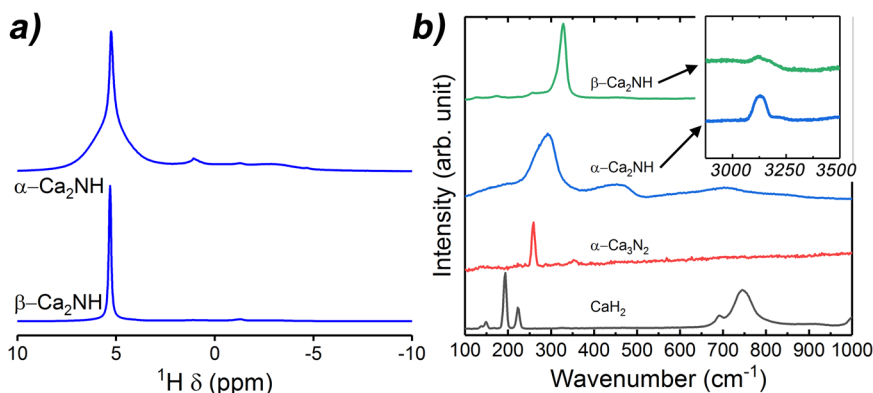


Fig. 2 | NMR and Raman spectra for the Ca₂NH phases. **a** NMR results collected on the α - and β -phases of Ca₂NH. Spectra show the ordering difference between the two phases that likely results from the presence of a secondary anion species. This disordering is manifested as a broadened H⁺ signal (5.2 ppm) at room temperature as well as the presence of other peaks associated with amide (1.0 ppm) and imide species (-2.7 ppm). **b** Raman Results collected on precursors and α - and β - phases

of Ca₂NH. The spectra also show that the main band associated with the nitride-hydride at -300 cm⁻¹ is broadened and shifted to lower energies for the α -phase. Furthermore, the presence of a peak at 3125 cm⁻¹ confirms the presence of imide protons in the α -phase. There is also a small peak for the β - at this wavenumber but it is relatively weak implying that the relative concentration is low.

l extracted from the CEM. The results show that the l values are close to the octahedral site to site distances. Therefore, conductivity values were calculated for a H1-H1 pathway using the Einstein Diffusion equation in conjunction with the Nernst-Einstein equation:

$$D_{QENS} = \frac{l^2}{n\tau} \quad (1)$$

$$\sigma_{QENS} = D_{QENS} \frac{n_i(z_i e)^2}{k_B T} \quad (2)$$

Where, n is 2x dimensionality of the diffusion process (e.g. one dimensional, two dimensional, or three dimensional), n_i is the number density of species i (atoms cm⁻³), and $z_i e$ is the charge of species i . The number densities were calculated from the NPD structure refinements

using the following equation:

$$n_i = \frac{m_i O_i}{V_{cell}} \quad (3)$$

Where m_i and O_i are the multiplicity and occupancy of a species in site i , and V_{cell} is the volume of the unit cell. The resulting σ_{QENS} values are significantly higher (-0.5 S cm⁻¹ for 3D diffusion, and -0.7 S cm⁻¹ for 2D) than the measured σ_{EIS} (-0.08 S cm⁻¹). However, it was noticed that if the n_{H2} (the number density of the tetrahedral site, see Supplementary Fig. 15) was used instead, then the conductivity values were much closer (-0.098 S cm⁻¹). Since, the n_{H2} site is associated with intrinsic anti-Frenkel defects, n_{H2} should reflect the vacancy concentration in the octahedral position ($n_{v,H1}$) for this β -Ca₂NH structure which refines as overall stoichiometric. Thus, a modified Nernst-Einstein equation that takes into account the fraction of charge carrier sites that have

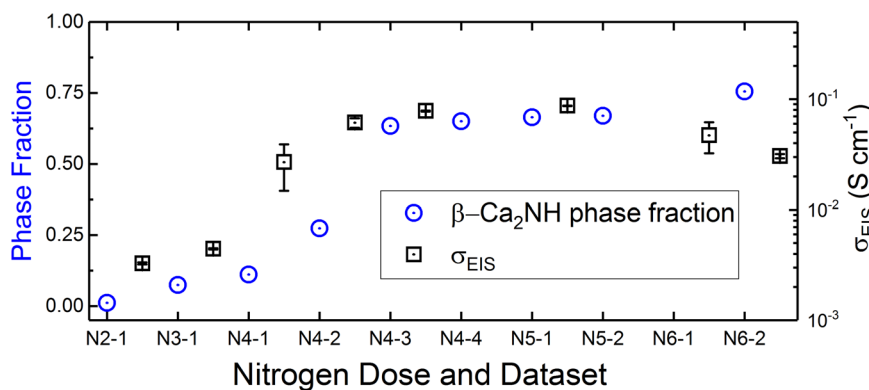


Fig. 3 | Ionic conductivity (σ_{EIS}) and phase fraction versus nitrogen doping. The data show that as the phase fraction of the nitride-hydride grows, so does the σ_{EIS} . The σ_{EIS} are offset to show that the values represent the average of the measured conductivities between diffraction experiments. The error bars represent one standard deviation. Notice that after dose 4 and the first diffraction dataset that a large error is present for σ_{EIS} . This error disappears when the phase fraction stabilizes sometime after the second diffraction pattern was taken (N4-2). The large change in EIS signal is shown in Supplementary Fig. 14. The next important

information in this figure is the drop in conductivity after the 6th dose. Upon the 6th dose of nitrogen the resistance associated with the sample–electrode interface grew dramatically probably a result of delamination. This resulted in the Rs value associated with the bulk conductivity being difficult to measure accurately (see Supplementary Fig. 14); allowing for only the first few datasets to be analysed. EIS results obtained in a separate experiment show that the σ_{EIS} is stable for β -Ca₂NH over long periods (see Supplementary Fig. 16).

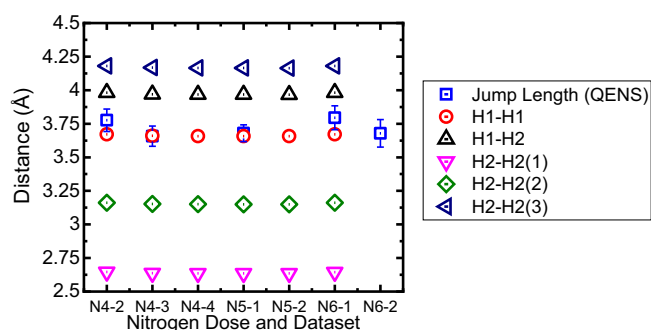


Fig. 4 | Jump length versus lattice distances. A plot of jump length (l) extracted from the quasi-elastic neutron scattering data via the Chudley–Elliott model³⁸ versus H site to site distances for β -Ca₂NH at 600 °C. Results show that the jump length is close to the H1 to H1 site to site distance implying that the diffusive motion takes place via octahedral site to octahedral site jumps. Error bars represent one standard deviation.

neighbouring vacancies ($\chi_{i,vac}$) was employed:

$$\sigma_{QENS} = D_{QENS} \frac{n_i(z_i e)}{k_B T} \chi_{i,vac} \quad (4)$$

There are two equivalent ways to think about the effect of this term. First, one can consider an *effective* charge carrier concentration:

$$n_i \chi_{i,vac} = n_{i,eff} \quad (5)$$

In this case, $n_{i,eff}$ defines the number of atoms in site i that have a neighboring vacancy and thus are able to diffuse. The second way is to define D_H (diffusion coefficient for H) from D_{QENS} (the diffusion coefficient as measured by QENS). Since QENS broadening only occurs due to dynamic motion, the QENS technique is only sensitive to the individual atoms that are mobile (either locally or over long range). In this case, the mobile atoms are the atoms with neighbouring vacancies which means that QENS is actually measuring the diffusion coefficient of the vacancies (D_{vac}). This term can be related to the diffusion coefficient of H (D_{H^-}) via the

following relations:

$$D_{i,vac} n_{i,vac} = D_i n_i \quad (6)$$

$$\frac{n_{i,vac}}{n_i} = \chi_{i,vac} \quad (7)$$

$$D_{i,vac} \chi_{i,vac} = D_i \quad (8)$$

Hence, Eq. 4 is modified to be either expressed as function of D_{H^-} or as a function of $n_{i,vac}$. The NPD structure refinements returned a vacancy concentration of 18.9% ($\chi_{vac} = 0.189$) for β -Ca₂NH. When this equation is applied to the H1 sites, the agreement between the σ_{QENS} and σ_{EIS} becomes remarkable (see Fig. 5 insert). The error associated with the refinement of the occupancy was just 1.3%. Thus the combined QENS and EIS data point to a vacancy mediated conductivity pathway for β -Ca₂NH. Furthermore, the results show that a 3D model results in a significantly better fit than a 2D model indicating that the arrangement of octahedral sites agrees with the $Fd-3m$ space group, rather than the 2D hydride array predicted by $R-3m$. This result also explains why the α -phase has poor ionic conductivity: there are no vacancies in the octahedral sites likely as a result of the entropic contribution of the imide species (i.e. the observed broadness of the NMR peak at room temperature for the α -). A similar result is seen in the difference in conductivity between lithium imide (Li₂NH, $Fd-3m$) and lithium amide (LiNH₂, $I-4$) where the former showed good conductivity properties due to the creation of 2 Frenkel pair defects^{39,40}, similar to what we see here.

Comparing the results of this combined in situ QENS and EIS experiment with previously published research on BaH₂ shows that the D_{QENS} measured for the β -Ca₂NH system is higher than that measured for BaH₂²⁹; while the overall conductivity at 600 °C for the two systems is significantly higher for BaH₂—the difference arising from the significantly higher effective charge carrier concentrations in the BaH₂ due to the presence of a concerted migration mechanism. Table 2 summarizes the difference between the two systems. Thus, while both these systems are fast hydride ion conductors, the mechanisms by which they achieve this are vastly different.

We have presented the H⁻ ion conductor β -Ca₂NH and also shown that the closely related α -phase (containing disorder due to the presence of secondary anionic species) has poor ionic conductivity

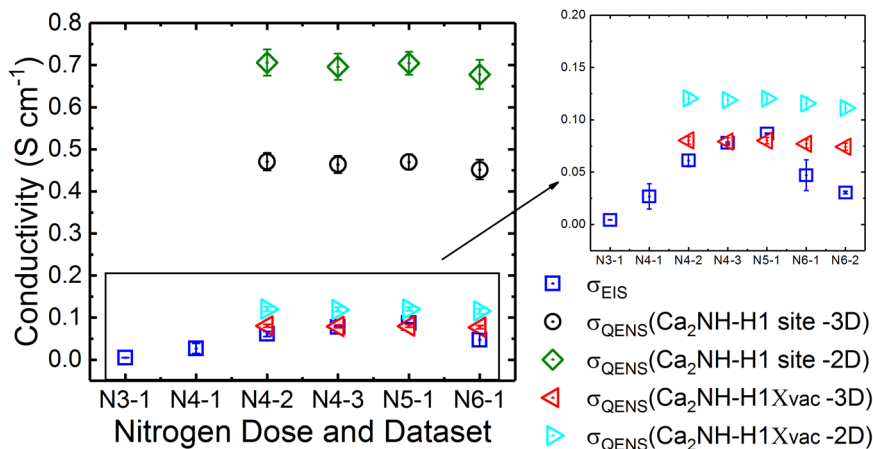


Fig. 5 | Conductivity comparison from different techniques. The results show that a 2D and 3D pathway for the HI site results in a predicted ionic conductivity for the quasi-elastic neutron scattering (QENS) data that is significantly higher than that measured by impedance spectroscopy (EIS) (0.08 S cm^{-1} vs 0.7 S cm^{-1} for 2D and 0.5 S cm^{-1} for 3D). However, if the probability of the a 1H site having a neighboring vacancy is taken into account (see Eqs. 4–6) then the 3D pathway QENS

calculated value agree remarkably well with the EIS measured conductivity (for N5–1, 0.080 S cm^{-1} for QENS versus 0.084 S cm^{-1} for EIS). This result implies a vacancy mediated diffusion mechanism. It is believed that difference between the techniques for the 6th nitrogen dose arises due to issues with the electrode–sample interface. This explored further in Supplementary Fig. 14. Error bars represent one standard deviation.

Table 2 | A comparison between two hydride ion conductors

System @ 600 °C	$n_{\text{H}} \text{ (cm}^{-3}\text{)}$	$\sigma \text{ (S cm}^{-1}\text{)}$	$D \text{ (cm}^2 \text{ s}^{-1}\text{)}$
BaH ₂	$1.50 \text{ (2)} \times 10^{22}$	0.32 (3)	$1.17 \text{ (3)} \times 10^{-5}$
β -Ca ₂ NH	$2.31 \text{ (5)} \times 10^{21}$	0.0782 (3)	$1.63 \text{ (6)} \times 10^{-5}$
ratio	6.5	4.0	0.72

Although, calcium nitride-hydride has a higher diffusion coefficient than barium hydride²⁹, its overall conductivity is significantly lower due to the almost 10x lower effective charge carrier concentration. The dramatic difference in this concentration is due to the different driving mechanisms for diffusion. Standard Error are shown in parentheses and correspond to the smallest magnitude numeral.

potentially as a result of the lack of intrinsic vacancies caused by the presence of the imide species in the phase; this result has important implications for MCAS in that the ionic conductivity of the support material may play a fundamental role in promoting the TM catalyst via the removal of adatoms from the surface. This is evinced by the Mars-van Krevelen mechanism observed by Kitano et al. and by the chemical looping of BaH₂ systems by Gao et al.^{4,7}, both implying significant contributions to the overall process from the bulk of the N–H support materials.

This paper has provided direct evidence for a vacancy-mediated conductivity pathway by using combined analysis of simultaneously collected QENS and EIS data. Finally, this paper has shown that secondary characteristic techniques such as NMR and Raman are important to verifying and understanding the crystal structure of N–H materials.

Methods

All materials were handled under Ar atmosphere, as the samples are air-sensitive. Under these conditions, the phases are stable.

Neutron powder diffraction

CaD₂ was synthesized from pure calcium shot in a sealed reactor at 800 °C for 6 h under flowing 5% D₂ in Ar at $100 \text{ cm}^{-3} \text{ min}^{-1}$. 25 mm pellets were pressed of CaD₂ and α -Ca₃N₂ (purchased from Alfa Aesar >99%) and sintered at 800 °C for 2 h under flowing 5% D₂ / N₂ respectively in Ar at $100 \text{ cm}^{-3} \text{ min}^{-1}$. The sintered pellets were then painted with palladium ink (C2031105P2) from Gwent Group and the electrodes were dried inside an oven in a glovebox at 100 °C for 10 min.

A microscopic camera was used to photograph the electrodes along with a calibration slide. These pellets were loaded into a specialized in situ cell (the St Andrews in situ cell) at ISIS inside a glovebox and then placed inside the RAL4 furnace loaded on Polaris²⁸. All diffraction data structures were refined using GSAS⁴¹.

Quasi-elastic neutron scattering experiment

CaH₂ was purchased from Fluka. A 25 mm pellet of CaH₂ was prepared in identical manner as the NPD experiment (with the substitution of H₂ for D₂) except the pellet was extremely thin to allow for the 90% transmission rule (e.g. a rule of thumb to reduce signal to noise ratio). The St Andrews in situ rig was used again but this time in conjunction with the RAL3 furnace and the Osiris spectrometer at ISIS³⁷. Simultaneous EIS, diffraction, and QENS data were collected. The sample was oriented at a 45° angle to the incoming neutron beam to maximize the exposed sample area. The sample was heated to 600 °C under flowing Ar and H₂ (95 and $5 \text{ cm}^{-3} \text{ min}^{-1}$ respectively). A Solartron 1280Z was used to collect EIS data with a 40 mV perturbation voltage between 20 kHz and 1 Hz.

NMR and Raman experiments

α -Ca₂NH and β - were synthesized at St Andrews at 600 °C with exposure to $5/5/90 \text{ cm}^{-3} \text{ min}^{-1}$ N₂/ H₂/ Ar for the nitride and hydride precursors. These materials were loaded into air-tight sample holders inside a glovebox and then transported to the NMR and Raman facilities. The NMR spectra were collected on a 9.4 T spectrometer with a magic angle spin of 14 kHz. The Raman spectra were collected using Renishaw inVia Raman Microscope with a 532 nm laser at 5% power collected over 10 s from 100 cm^{-1} to 3500 cm^{-1} .

Data availability

The research data underpinning this publication can be accessed at <https://doi.org/10.17630/6760d05d-114b-47ee-99bf-c9481cf25a55>. For neutron data see refs. 42–44.

References

- Kitano, M. et al. Self-organized ruthenium-barium core-shell nanoparticles on a mesoporous calcium amide matrix for efficient low-temperature ammonia synthesis. *Angew. Chem. Int. Ed.* **57**, 2648–2652 (2018).

2. Tang, Y. et al. Metal-dependent support effects of oxyhydride-supported Ru, Fe, Co catalysts for ammonia synthesis. *Adv. Energy Mater.* **8**, 1–9 (2018).
3. Hattori, M. et al. Enhanced catalytic ammonia synthesis with transformed BaO. *ACS Catal.* **8**, 10977–10984 (2018).
4. Gao, W. et al. Production of ammonia via a chemical looping process based on metal imides as nitrogen carriers. *Nat. Energy* **3**, 1067–1075 (2018).
5. Abe, H. et al. Anchoring bond between Ru and N atoms of Ru/Ca 2 NH catalyst: crucial for the high ammonia synthesis activity. *J. Phys. Chem. C* **121**, 20900–20904 (2017).
6. Wang, P. et al. Breaking scaling relations to achieve low-temperature ammonia synthesis through LiH-mediated nitrogen transfer and hydrogenation. *Nat. Chem.* <https://doi.org/10.1038/nchem.2595> (2017).
7. Kitano, M. et al. Essential role of hydride ion in ruthenium-based ammonia synthesis catalysts. *Chem. Sci.* **7**, 4036–4043 (2016).
8. Inoue, Y. et al. Efficient and stable ammonia synthesis by self-organized flat Ru nanoparticles on calcium amide. *ACS Catal.* **6**, 7577–7584 (2016).
9. Abild-Pedersen, F. et al. Scaling properties of adsorption energies for hydrogen-containing molecules on transition-metal surfaces. *Phys. Rev. Lett.* **99**, 4–7 (2007).
10. Gao, W. et al. Barium Hydride-Mediated Nitrogen Transfer and Hydrogenation for Ammonia Synthesis: A Case Study of Cobalt. *ACS Catal.* **7**, 3654–3661 (2017).
11. Verbraeken, M. C., Cheung, C., Suard, E. & Irvine, J. T. S. High H-ionic conductivity in barium hydride. *Nat. Mater.* **14**, 95–100 (2015).
12. Takeiri, F. et al. Hydride-ion-conducting K₂NiF₄-type Ba–Li oxyhydride solid electrolyte. *Nat. Mater.* **21**, 325–330 (2022).
13. Fukui, K., Iimura, S., Iskandarov, A., Tada, T. & Hosono, H. Room-temperature fast H-conduction in oxygen-substituted lanthanum hydride. *J. Am. Chem. Soc.* **144**, 1523–1527 (2022).
14. Ooya, K. et al. Ruthenium catalysts promoted by lanthanide oxyhydrides with high hydride-ion mobility for low-temperature ammonia synthesis. *Adv. Energy Mater.* **11**, 1–12 (2021).
15. Kobayashi, Y. et al. Titanium-based hydrides as heterogeneous catalysts for ammonia synthesis. *J. Am. Chem. Soc.* **139**, 18240–18246 (2017).
16. Kitano, M. et al. Low-temperature synthesis of perovskite oxynitride-hydrides as ammonia synthesis catalysts. *J. Am. Chem. Soc.* **141**, 20344–20353 (2019).
17. Brice, J. F., Motte, J. P., Courtois, A., Protas, J. & Aubry, J. Etude structurale de Ca₂NH par diffraction des rayons X, diffraction des neutrons et resonance magnetique nucléaire du proton dans le solide. *J. Solid State Chem.* **17**, 135–142 (1976).
18. Verbraeken, M. C., Suard, E. & Irvine, J. T. S. Order and disorder in Ca₂NDO.90HO.10—A structural and thermal study. *J. Solid State Chem.* **184**, 2088–2096 (2011).
19. Altorfer, F. et al. H–jump diffusion in barium-nitride-hydride Ba₂NH. *Solid State Ion.* **70–71**, 272–277 (1994).
20. Sichla, T. et al. Crystal structure determination of a strontium hydride imide nitride—Sr₂(H)N/SrNH resp. Sr₂(D)N/SrD- by x-ray, neutron, and synchrotron radiation. *Zeit. Anorg. Allg. Chem.* **623**, 414–422 (1997).
21. Chemnitzer, R., Auffermann, G., Többens, D. M. & Kniep, R. (Sr₂N)H: Untersuchungen zur redox-intercalation von wasserstoff in Sr₂N. *Zeit. Anorg. Allg. Chem.* **631**, 1813–1817 (2005).
22. Ravi, M. & Makepeace, J. W. Lithium-nitrogen-hydrogen systems for ammonia synthesis: exploring a more efficient pathway using lithium nitride-hydride. *Chem. Commun.* **58**, 6076–6079 (2022).
23. Makepeace, J. W. et al. Compositional flexibility in Li–N–H materials: implications for ammonia catalysis and hydrogen storage. *Phys. Chem. Chem. Phys.* **23**, 15091–15100 (2021).
24. Weidner, E. et al. Observation of novel phases during deuteration of lithium nitride from in situ neutron diffraction. *Chem. Phys. Lett.* **444**, 76–79 (2007).
25. Mizoguchi, H. et al. Hydride-based electride material, LnH₂ (Ln = La, Ce, or Y). *Inorg. Chem.* **55**, 8833–8838 (2016).
26. Xiong, Z., Chen, P., Wu, G., Lin, J. & Lee Tan, K. Investigations into the interaction between hydrogen and calcium nitride. *J. Mater. Chem.* **13**, 1676–1680 (2003).
27. Michalsky, R., Avram, A. M., Peterson, B. A., Pfromm, P. H. & Peterson, A. A. Chemical looping of metal nitride catalysts: Low-pressure ammonia synthesis for energy storage. *Chem. Sci.* **6**, 3965–3974 (2015).
28. Smith R. I., et al. The upgraded Polaris powder diffractometer at the ISIS neutron source. *Rev. Sci. Instrum.* **90**, 115101 (2019).
29. Irvine, G. J. et al. Geometric frustration and concerted migration in the superionic conductor barium hydride. *Chem. Mater.* **34**, 9934–9944 (2022).
30. Sichla, T. & Jacobs, H. ChemInform abstract: synthesis and crystal structure of calcium imide, CaNH. *ChemInform* <https://doi.org/10.1002/chin.199714007> (2010).
31. Chen, P., Xiong, Z., Luo, J., Lin, J. & Tan, K. L. Interaction of hydrogen with metal nitrides and imides. *Nature* **420**, 302–304 (2002).
32. David, W. I. F. et al. A mechanism for non-stoichiometry in the lithium amide/lithium imide hydrogen storage reaction. *J. Am. Chem. Soc.* **129**, 1594–1601 (2007).
33. Verbraeken, M. C., Suard, E. & Irvine, J. T. S. Structural and electrical properties of calcium and strontium hydrides. *J. Mater. Chem.* **19**, 2766 (2009).
34. Wegner, B., Essmann, R., Bock, J., Jacobs, H. & Fischer, P. Structure and H-ionic-conductivity of barium hydride nitrid, Ba₂H(D)N. *Eur. J. Solid State Inorg. Chem.* **29**, 1217–1227 (1992).
35. Apperley, D. C., Harris, R. K. & Hodgkinson, P. *Solid-State NMR: Basic Principles and Practice* (Momentum Press, 2012).
36. Hull, S. Superionics: crystal structures and conduction processes. *Rep. Prog. Phys.* **67**, 1233–1314 (2004).
37. Telling, M. T. F. & Andersen, K. H. Spectroscopic characteristics of the OSIRIS near-backscattering crystal analyser spectrometer on the ISIS pulsed neutron source. *Phys. Chem. Chem. Phys.* **7**, 1255–1261 (2005).
38. Chudley, C. T. & Elliott, R. J. Neutron scattering from a liquid on a jump diffusion model. *Proc. Phys. Soc.* **77**, 353–361 (1961).
39. Miceli, G., Cucinotta, C. S., Bernasconi, M. & Parrinello, M. Correction to “first principles study of the LiNH₂/Li₂NH transformation”. *J. Phys. Chem. C* **116**, 2645–2645 (2012).
40. Li, W., Wu, G., Xiong, Z., Feng, Y. P. & Chen, P. Li + ionic conductivities and diffusion mechanisms in Li-based imides and lithium amide. *Phys. Chem. Chem. Phys.* **14**, 1596–1606 (2012).
41. Toby, B. H. EXPGUI, a graphical user interface for GSAS. *J. Appl. Crystallogr.* **34**, 210–213 (2001).
42. Irvine, G. J., Carins, G. M., Smith, R. I., Jones, M. O. & Irvine, J. T. In-situ hydrogenation of calcium nitride. *STFC ISIS Neutron and Muon Source Data J.* <https://doi.org/10.5286/ISIS.E.RB1720395> (2018).
43. Carins, G. M. et al. In situ studies of conduction mechanisms and nitrogen incorporation in alkaline earth deuterides. *STFC ISIS Neutron and Muon Source Data J.* <https://doi.org/10.5286/ISIS.E.53840907> (2014).
44. Irvine, G. J., Carins, G. M., Demmel, F., Owen Jones, M. & Irvine, J. T. S. In-situ QENS studies of the nitridation of calcium hydride. *STFC ISIS Neutron and Muon Source Data J.* <https://doi.org/10.5286/ISIS.E.87778661> (2017).

Acknowledgements

Neutron scattering beamtime (RB1720395⁴², RB1410181⁴³, RB1720393⁴⁴) at the ISIS neutron and muon source was provided by the UK Science and Technology Facilities Council (STFC). Prof John TS Irvine and Prof Martin Owen Jones: STFC 5005—Development of Combined In situ Neutron Diffraction and Electrochemical Studies. We thank Dr Daniel Dawson for assistance with Solid State NMR data collection at St Andrews.

Author contributions

G.J.I.: manuscript, data collection and analysis. R.I.S.: Neutron diffraction data experiments setup and collection/reduction. M.O.J.: main author's academic advisor, and conceptualisation. J.T.S.I.: main author's academic advisor, editing and conceptualisation.

Competing interests

The authors declare no competing interests.

Additional information

Supplementary information The online version contains supplementary material available at <https://doi.org/10.1038/s41467-023-40025-2>.

Correspondence and requests for materials should be addressed to G. J. Irvine or J. T. S. Irvine.

Peer review information *Nature Communications* thanks Josh

Makepeace, Hideo Hosono and the other, anonymous, reviewer(s) for their contribution to the peer review of this work. A peer review file is available.

Reprints and permissions information is available at <http://www.nature.com/reprints>

Publisher's note Springer Nature remains neutral with regard to jurisdictional claims in published maps and institutional affiliations.

Open Access This article is licensed under a Creative Commons Attribution 4.0 International License, which permits use, sharing, adaptation, distribution and reproduction in any medium or format, as long as you give appropriate credit to the original author(s) and the source, provide a link to the Creative Commons licence, and indicate if changes were made. The images or other third party material in this article are included in the article's Creative Commons licence, unless indicated otherwise in a credit line to the material. If material is not included in the article's Creative Commons licence and your intended use is not permitted by statutory regulation or exceeds the permitted use, you will need to obtain permission directly from the copyright holder. To view a copy of this licence, visit <http://creativecommons.org/licenses/by/4.0/>.

© The Author(s) 2023